



LAWRENCE
LIVERMORE
NATIONAL
LABORATORY

Backlighter development at the National Ignition Facility (NIF): Zinc to Zirconium

M. A. Barrios, K. B. Fournier, S. P. Regan, O. Landen,
M. May, Y. P. Opachich, K. Widmann, D. K. Bradley, G.
W. Collins

June 6, 2013

High Energy Density Physics

Disclaimer

This document was prepared as an account of work sponsored by an agency of the United States government. Neither the United States government nor Lawrence Livermore National Security, LLC, nor any of their employees makes any warranty, expressed or implied, or assumes any legal liability or responsibility for the accuracy, completeness, or usefulness of any information, apparatus, product, or process disclosed, or represents that its use would not infringe privately owned rights. Reference herein to any specific commercial product, process, or service by trade name, trademark, manufacturer, or otherwise does not necessarily constitute or imply its endorsement, recommendation, or favoring by the United States government or Lawrence Livermore National Security, LLC. The views and opinions of authors expressed herein do not necessarily state or reflect those of the United States government or Lawrence Livermore National Security, LLC, and shall not be used for advertising or product endorsement purposes.

Backlighter development at the National Ignition Facility (NIF): Zinc to Zirconium

M. A. Barrios¹, K. B. Fournier¹, S.P. Regan², O. Landen¹, M. May¹, Y. P. Opachich¹, K. Widmann¹, D. K. Bradley¹, and G. W. Collins¹

¹Lawrence Livermore National Laboratory, Livermore, California 94550, USA

²Laboratory for Laser Energetics, University of Rochester 250 East River Road, Rochester, NY 14623-199, USA

Abstract

K-shell x-ray emission from laser-irradiated planar Zn, Ge, Br, and Zr foils was measured at the National Ignition Facility for laser irradiances in the range of 0.6 to 9.5×10^{15} W/cm². The incident laser power had a pre-pulse to enhance the laser-to-x-ray conversion efficiency (CE) of a 2 to 5 ns constant-intensity pulse used as the main laser drive. The measured CE into the 8 to 16 keV energy band ranged from 0.43% to 2%, while the measured CE into the He-like resonance $1s^2$ – $1s2p(1P)$ and intercombination $1s^2$ – $1s2p(3P)$ transitions, as well as from their $1s^2(2s,2p)^l$ – $1s2p(2s,2p)^l$ satellite transitions for $l = 1, 2, 3$, corresponding to the Li-, Be-, and B-like resonances, respectively, ranged from 0.3% to 1.5%. Absolute and relative CE measurements are consistent with x-ray energy scaling of $(h\nu)^{-3}$ to $(h\nu)^{-5}$, where $h\nu$ is the x-ray energy. The temporal evolution of the broadband x-ray power was similar to the main laser drive for ablation plasmas having a critical density surface.

1. Introduction

X-ray radiography is a powerful diagnostic technique for inertial confinement fusion (ICF) and high-energy-density (HED) plasmas. The areal density of compressed targets can be probed with x-ray radiography to study imploding ICF targets, material interface instabilities, and radiative shocks.[1–8] The quality of the data extracted from a radiograph depends on the photon energy of the backlighter and the x-ray source brightness. The photon energy dictates the x-ray penetration depth in the target and affects the image contrast. Source brightness ensures adequate x-ray fluence is incident on the detector. This is especially important for experiments requiring high magnification, such as ICF experiments. The brightness and photon energy of the backlighter need to be optimized for the areal density under consideration.

X-ray radiography is used at the National Ignition Facility (NIF) [9,10] to measure the trajectory of the compressed-shell areal density as the shell implodes, leading to estimates of the shell velocity and the ablator mass remaining.[8] These are critical metrics of the implosion dynamics. As the shell converges its areal density increases. For times leading up to stagnation, higher photon energies are needed to probe the shell's increasing areal density. Initial x-ray radiography experiments for ICF implosions probed the shell at early times in the trajectory using a 5 μ m thick Zn planar foil driven with ~ 32 kJ delivered in a 1 or 2 ns square pulse to produce an 8.9 keV backlighter. Current experiments need to probe capsules with higher fractions of high-Z ablator dopants, as well as investigate capsule conditions at times closer to stagnation. These experiments require a higher-photon-energy backlighter source with conversion efficiency of $\sim 1\%$, due to expected contrast and required signal-to-background ratio. This is particularly challenging because for fixed incident laser irradiance the laser-to-x-ray conversion efficiency decreases markedly for increasing backlighter photon energy.[11–14] Additionally, the sensitivity of x-ray

photocathodes decreases for increasing photon energy, necessitating higher photon throughput at the detector [15].

This study characterizes laser-irradiated, planar foil x-ray backlighters that will be used in radiographic measurements of imploding ICF targets on NIF. Spectrally resolved and broadband x-ray measurements were used to determine laser-to-x-ray conversion efficiencies for zinc ($Z=30$), germanium ($Z=32$), bromine ($Z=35$) and zirconium ($Z=40$) targets (see **Table 1**). The laser configuration, target design, and diagnostics fielded for these experiments are described in Section 2. In Section 3 we discuss the measured results, followed by the conclusions.

2. Experimental Method

The experiments were performed at the National Ignition Facility (NIF) [9,10], employing a frequency-tripled 351 nm, 1.8 MJ, 192 beam Nd:YAG laser. The backlighter planar-foil targets were driven with up to eight beams delivering 16-60 kJ of energy (typically 2.2 TW per beam), with a laser drive similar to the backlighter beam configuration used for implosion-radiograph experiments at NIF.[16,17] Pulse shapes used in these experiments are shown in Fig. 1. For a subset of experiments two different plasma conditions were tested simultaneously by irradiating spatially distinct sections of the target, each with four beams. The remaining experiments focused eight laser beams onto a single region of the planar foil target. All beams were incident on the foil at a 40° angle relative to the foil normal. The laser focal spot intensity profiles were smoothed using phase plates [18], generating a nearly elliptical uniform irradiation area either $0.8 \times 1.2\text{mm}$ or $270 \times 400\mu\text{m}$, with peak target irradiances in the 0.6 to $9.5 \times 10^{15} \text{ W/cm}^2$ range. A pre-pulse followed by a nominally constant-intensity main drive, having a duration between 2 to 5 ns, was used to produce multi-keV K-shell emission from the target. Irradiating the target foil with a pre-pulse creates a larger underdense plasma ($n_e/n_{cr} \approx 0.1-0.2$, where n_{cr} is the critical density for absorption of the laser energy by the plasma), enabling the plasma to ionize more efficiently once the main drive arrives [19–21]. The underdense plasma is able to absorb a larger fraction of thermal energy via inverse bremsstrahlung, in comparison to a target irradiated by a main pulse without a pre-pulse, because the pre-pulse generates a larger absorption volume that is less susceptible to hydrodynamic losses, which lower the conversion efficiency into radiation. [20,22,23]. Based on the results from previous work [22] the main drive was delayed by 3 ns relative to the pre-pulse, see Fig. 1. The pre-pulse had a temporal width of ~ 700 ps, peaking at 0.5 TW per beam for most shots. Figure 2 shows a schematic of the experimental configuration indicating the diagnostics used to measure target x-ray yield. Targets consisted of 5 to 12 μm thick, $3 \times 3\text{mm}$ square foils (see

Table 1) aligned to target chamber center. A gold mask with a slit 2mm long and 5 to 17 μm in width, as shown in Fig. 2, or an $800 \times 925 \mu\text{m}$ aperture was attached to the target stalk ~ 2 mm from the foil, opposite the drive beams. These masks are used as a limiting aperture, imitating features in the hohlraums of 1-D streaked and 2-D gated implosion radiograph targets, respectively. The surface normal of the planar mask is angled 18° with respect to the photodetector line of sight, to prevent debris from the mask hitting the x-ray photodetector.

As seen in Fig. 2, a suite of x-ray diagnostics, consisting of a time-integrated x-ray spectrometer, a broadband time-resolved x-ray photodiode and a broadband x-ray imaging streak camera, was used to characterize the backlighter spectral content and x-ray power output. One-dimensional (1-D), time-integrated, absolutely calibrated spectral images of the laser irradiated planar foils were recorded with the SuperSnout II spectrometer (SSIIS) [24] The SSIIS has four elliptical PET crystals[25] defining four independent spectral

channels with overlapping photon energies covering the spectral range from 6-16 keV. The 1-D imaging is achieved with a 100 μm wide slit located near the target with its length lying in the plane of dispersion. The standoff distance between the target and the entrance aperture is varied to achieve a magnification of 4x or 12x in the 1-D spectral image. Both magnifications were used during these experiments. Each channel can be individually filtered to adjust the signal levels on the image plate detector. The instrument response function of the SSIIS uses the measured integrated reflectivity of the PET crystals[26], the SR image plate sensitivity and fade correction calibrated by Maddox et al. [27], and published filter transmissions[24]. The spectral resolving power, E/dE , where E is the spectral energy, of the SSIIS varies from 100 to 400 for mm-scale x-ray sources[24]. Its line of sight was at 90° with respect to the target normal, looking at the foil edge-on, with its imaging direction at a 34° angle with respect to the foil edge; the 1-D spatial resolution axis was not aligned to resolve the emission from two distinct laser drive conditions incident on some of the planar foils.

The spectral content emitted by the laser-irradiated foil was also quantified using Dante [28,29], an 18 channel filtered x-ray diode array. Each Dante channel records the time-resolved x-ray emission for a given spectral bandwidth, determined by the diode response function and the x-ray transmission of the foil filters. Dante views the laser irradiated surface of the target at a $\sim 54^\circ$ angle relative to the foil normal, see Fig. 2. All Dante diodes and filters are calibrated prior to use providing absolute x-ray flux measurements.[30] The SSIIS and Dante record spatially-integrated spectra.

The backlighter temporal and 1-D spatial x-ray emission uniformity, viewed parallel to the foil normal, was quantified using the Diagnostic Insertion Manipulator Imaging Streak Camera (DISC)[31–33]. Using a 500 μm slit the DISC has a temporal resolution of 32 ps and 76 ps for the 2 ns and 5 ns sweep speeds, respectively, and a 1-D spatial resolution of 70 μm at the photocathode. For experiments using two spatially separated laser drive conditions, the DISC imaging diagnostic spatially resolves the plasmas formed by each laser configuration. The DISC was run with a 2 ns or 5 ns temporal window at 5.2X, 7.8X, or 9X magnification.

Figure 3 shows the x-ray images of emission above 6 keV resulting from various laser irradiance schemes. A time-integrated static x-ray imager views the target, located at target chamber center, from a (θ, φ) position of $(161^\circ, 236^\circ)$ looking at the target nearly edge-on, see Fig. 3(a). The first configuration (from left to right) in Fig. 3(b) corresponds to a 3ns main drive, with the bottom half of the target using a 400 μm diameter laser spot, using 400 μm continuous phase plates (CPP's), and the top half of the target using an elliptical projected laser spot with minor and major axes of 0.8mm and 1.2mm, respectively (using Scl-1 CPP's). A significantly smaller plasma plume, both along and perpendicular to the target surface is observed when using 400 μm CPP's. The second and third images used Scl-1 CPP's with a 3ns and 5ns pulse with 4 beams each, and a 2ns main drive using 8 beams. These images show the plasma size parallel to the foil, corresponding to half peak emission, closely follows the irradiance spot size, measuring between 1.2 to 1.3 mm for Scl-1 CPP's spots, and 600 μm for the 400 μm CPP's case. The plume expansion normal to the foil surface was $\sim 400 \mu\text{m}$ and 200 μm for Scl-1 CPP's and 400 μm CPP's, respectively.

3. Data Analysis and Results

3.1. Conversion efficiency into He_α and satellite emission

Figure 4 shows time-integrated spectra measured with SSIIS for a Zn, Ge, and Br shot. Spectral data recorded for channel-1 (5.8 to 10.1 keV), -2 (6.4 to 11.2 keV), -3 (7.2 to 12.7 keV), and -4(9.3 to 16.5 keV) are shown as the dotted, dashed, dot-dashed, and solid curves. Measurements show He-like emission dominates the K-shell spectrum for all three

materials, in Fig. 4 (a) and (b) we can identify the He_α , He_β , and He_γ line emission for Zn and Ge, and in Fig. 4 (c) we observe the He_α and He_β line emission for Br. Zn and Ge foils reach hydrogen-like ion stage, as the Ly_α emission can be observed in the spectra in Fig. 4 (a) and (b). The spectra in Fig. 4 demonstrate good agreement for the channels that have overlapping spectral ranges, providing an in-situ check on the instrument's spectral calibration. Note also that for the Zn and Ge data the SSIIS spectral resolution is sufficiently high enough to resolve satellite lines on the low-energy side of the He_β line.

The Zr He_α line, at 16.3 keV, falls too close to the upper photon limit range of the SSIIS to record the full line width of this feature in a first-order Bragg reflection. Instead the second-order Bragg reflection of the Zr He_α line was recorded on channels -1, -2, and -3. An in-situ calibration for second-order Bragg reflection was derived using the krypton He_β (15.4 keV) line, measured in first- and second-order Bragg reflection in a previous experiment. Here it is assumed that the integrated first- and second-order reflectivities are slowly varying between 15.4 to 16.3 keV such that calibration values at 15.4 keV can be applied to Zr He_α at 16.3 keV. Figure 5 shows the measured Zr He_α line profile after subtraction of the local continuum, corrections due to IP sensitivity, filter transmission, and scaled based on second-order calibration.

Laser-to-x-ray conversion efficiencies (CE) into He_α as a function of peak laser irradiance, measured for Zn (diamond), Ge (squares), Br (triangle), and Zr (circles) foils are shown in Fig. 6 as the filled symbols. For each channel the absolute brightness (J/keV/sr) of the He_α spectral line and its satellite emission, with the x-ray continuum subtracted, is integrated over the line width and over the 4π volume to determine the absolute yield (J). Here the local continuum is modeled as $I_0 e^{-h\nu/T}$ [34], where I_0 and T are used as fitting parameters. Inferred temperatures vary between 1-2 keV, and are listed in **Table 2**. These temperatures are lower than expected for generating He_α , therefore may reflect the cooler L-shell recombining phases of these plasmas. Uncertainty in this measurement includes the uncertainty in the fit between model and data, as well as variation in inferred T between channels. Preliminary analysis of measured line ratios using atomic physics codes indicates higher temperatures in the 4 to 6 keV range; a detailed description of this analysis and results will be presented in the future. Results in Fig. 6 correspond to the average CE and its standard deviation calculated from channels overlapping in spectral range. For Br, where He_α line emission was measured in channel-4 and only partially in channel-3, see Fig. 4, only data for channel-4 is reported with assigned 26% uncertainty based on results from other shots. CE values for Zr also include uncertainty from second-order calibration. For foils that were driven with two different laser configurations in spatially distinct regions of the foil, the CE is plotted at the average irradiance.

Laser-to-x-ray conversion efficiencies for the Ge data peaks at $1.5 \times 10^{15} \text{ W/cm}^2$ with an average CE of $(1.5 \pm 0.3)\%$. Data are compared with previous Ge results by Workman and Kyrala [14], shown as the open squares in Fig. 6. The latter study used Ge foils of similar thickness driven with a single-sided main drive, i.e., with no pre-pulse irradiation scheme. Fig. 6 shows significantly higher conversion efficiencies for Ge are achieved at lower laser irradiance for pre-pulsed foils. The highest CE measured for Zn in this study was $(1.1 \pm 0.3)\%$ at a laser irradiance of $2.0 \times 10^{15} \text{ W/cm}^2$. Data trends indicate that the optimum intensity for the Zn foil is likely to be at $\sim 1.0 \times 10^{15} \text{ W/cm}^2$. Zn pre-pulse foil data also show higher CE's are achieved at lower irradiances, in comparison to foils driven with a single main drive (open diamonds in Fig. 6).

Measured conversion efficiency of Zn and Ge foils at $0.5 \times 10^{15} \text{ W/cm}^2$ follow material Z-scaling of $(h\nu)^{-3}$ to $(h\nu)^{-4}$, where $h\nu$ is the nominal photon energy of the material's He_α emission, which is consistent with previously reported Z-scalings.[13,14] The Br target CE at $\sim 2.0 \times 10^{15} \text{ W/cm}^2$ was measured at $(0.3 \pm 0.1)\%$. Its low performance

relative to that measured for Zn (1.1%), Ge (1.3-1.5 %), and Zr ($0.5 \pm 0.1\%$) is attributed to the factor of 2 reduction in the number of available Br emitters, since the target used a KBr salt film.

For Zn and Ge foils SSIIS-derived CE into He_α can be compared with Dante fluxes, using a subset of isolated channels. These estimates include continuum emission and some residual energy outside of the spectral range of interest. Measurement uncertainties include variations in the channels response function over a 500 eV range as well as systematic uncertainties associated with Dante measurements, which will be discussed in Section 3.2. These Dante measurements are in close agreement with results from the SSIIS, and are given in Table 3.

3.2. Broadband (8.5 to 16 keV) conversion efficiency

Broadband (8.5 to 16 keV) laser-to-x-ray conversion efficiencies were characterized using Dante and SSIIS. Measured Dante voltages for a given channel i can be related to the source emitting area A and spectrum $S(E, t)$ GW/keV/sr, through [28,29,35]

$$V(t)_i = P_i \Omega_i A \cos(\theta) \int_0^\infty R(E)_i S(E, t) dE, \quad (1)$$

where P, Ω, θ and $R(E)$ represent the channel's electrical attenuation, solid angle, view angle relative to the source normal, and response function, respectively. The spectral band for each channel is determined by its filter, mirror, and diode combination. The source spectrum is derived using an iterative algorithm that minimizes residuals between measured and estimated channel voltages. The resulting spectra were time integrated to compare with SSIIS results.

Broadband measurements from SSIIS have a spectral bandwidth from 8.5 to 16keV. A full spectrum in this range was obtained by stitching data from all channels and averaging measured emission for spectral ranges where channel data overlap. A 26% error is taken for SSIIS data, based on errors derived for CE into He_α using overlapping channels. The Dante flux uncertainty is estimated by the method described by May et al. [28] and propagated through the time-integrated analysis. Uncertainty in the Dante-derived CE is estimated to be approximately 5%.

Results from broadband measurements are shown in Fig. 7 with Zn, Ge, Br, and Zr data again shown as diamonds, squares, triangles, and circles. Dante results are the filled symbols; SSIIS results are the unfilled symbols. CE values derived from SSIIS and Dante are provided in **Table 3**.

The SSIIS broadband data for Zn and Ge follow similar trends as CE results into He_α , as indicated in Fig. 6. Zn CE decrease for irradiances above $2.0 \times 10^{15} \text{ W/cm}^2$, while the Ge CE peaks at $\sim 1.5 \times 10^{15} \text{ W/cm}^2$, and quickly decrease at higher irradiances. At such irradiances it is likely a larger portion of the laser energy is generating hot electrons and these in turn are colliding with the target material to create hard x-rays ($>20 \text{ keV}$). [13] For Br both Dante and SSIIS broadband CE are comparable at $\sim 0.8\%$, close to 3 times higher than the measured CE into He_α , indicating the broadband signal is dominated by the low-energy continuum. Broadband CE measurements for Zr are around 0.43% and 0.36% for laser irradiances of 1.9 and $9.3 \times 10^{15} \text{ W/cm}^2$.

Figure 8 shows laser-to-x-ray conversion efficiency into He_α from this study (circles) in comparison to previous studies using hohlraum or halfraum targets [36,37] (rectangles), aerogel targets [38] (diamonds), single drive foils [13,14,39] (downward triangles), and pre-pulsed foils [22] (squares), spanning laser irradiances from 0.1 to $40 \times 10^{15} \text{ W/cm}^2$. Here the symbol shade (color online) depicts the laser irradiance used for each experiment. For experiments with unknown irradiance, symbols are unfilled. Results plotted in Fig. 8

show pre-pulse foils from this study reach higher CE than previous hohlraum/halfraum, single drive foil, and aerogel targets from previous experimental studies. Previous pre-pulsed [22] Ge foils measured a record CE $\sim 3\%$, higher than measured in this study. This previous work, however, used thinner $6\mu\text{m}$ samples in a double-sided irradiation configuration at ~ 3 times higher laser irradiance. No previous work is available for Br or Zr.

3.3. Relative conversion efficiency and Z-scaling

DISC data were used to obtain relative broadband x-ray to laser conversion efficiencies. Flat field and geometrical corrections were applied to the DISC images before extracting lineouts along the temporal axis, which were used to determine the average counts per pixel recorded by DISC over the main laser drive duration. Average counts for all shots were normalized to a 5-ns, 9X magnification DISC setup using a $17\mu\text{m}$ slit. In addition to the standard polyimide filtration, used to attenuate soft x-rays below ~ 6 keV and protect the camera from target debris, Zn, Ge, and Zr filters were used to attenuate x-rays above the Zn, Ge, and Br He_α . Corrections for filter transmission were applied at the foil material He_α energy. The number of x-ray photons incident on DISC's CsI photocathode was estimated by accounting for the CsI photocathode sensitivity, proportional to $(E - \zeta)^{0.3}/E^{2.8}$, where E is the photon energy and ζ is the L-shell ionization energy for CsI assumed to be 4.8 keV.[15,40–42] Multiplying by the He_α photon energy results in a relative x-ray yield that can be used to obtain relative CE.

Figure 9 shows broadband x-ray-to-laser conversion efficiencies measured with DISC. Error bars include statistical uncertainty associated with mean counts per pixel obtained from lineouts and estimated uncertainty in slit thickness based on contact radiograph analysis of the slits prior to DISC diagnostic-assembly. Data values are normalized to a single shot, N120812-001, which was a Ge foil driven with 1.45×10^{15} W/cm². Filled diamonds, squares, and triangles show relative CE for Zn, Ge, and Br foils, respectively.

Zn data at 0.57×10^{15} W/cm² show over a 30% increase in CE between $15\mu\text{m}$ (relative CE 0.84%) and $5\mu\text{m}$ (relative CE 1.2 %) thick foils. Within the range of irradiances spanned the broadband x-ray yield from Ge and Br foils increase with laser irradiance. In the case of Ge, where a peak in CE was observed in SSIIS and Dante data, this increasing trend in DISC-derived CE can be a compound effect due to filter transmission, which quickly increases after the Ge K-edge at 11.3 keV, and a larger production of high energy ($>16\text{keV}$) photons with increasing laser irradiance. High energy x-rays can be produced via bremsstrahlung radiation if a larger fraction of the incident laser energy goes into generating hot electrons that undergo collisional processes within the foil or substrate.

CE Z-scaling for three laser irradiances is shown in Fig. 10. The shaded regions bounded by dashed, solid, and dot-dashed lines respectively, represent $(h\nu)^{-3}$, $(h\nu)^{-4}$, and $(h\nu)^{-5}$ scalings set by DISC measurements and uncertainty. For each irradiance the data with smallest uncertainty were used as the scaling reference bound. Figure 10 (a) shows $12\mu\text{m}$ Ge foil measurements are consistent with $(h\nu)^{-3}$ to $(h\nu)^{-4}$ scaling with a similar thickness ($15\mu\text{m}$) Zn foil, and consistent with $(h\nu)^{-5}$ in comparison to a $5\mu\text{m}$ Zn foil. Comparison between Ge and Br foils, Fig. 10 (b) and (c), shows Z-scaling steepens with increasing laser irradiance from $\sim (h\nu)^{-4}$ to $\sim (h\nu)^{-5}$. These results are also consistent with previously reported scalings. [13,14]

3.4. X-ray power output

DISC measurements were also used to assess the backlighter temporal uniformity. Data traces for shots using $400\mu\text{m}$ CPP's driven with a 2.8 ns main drive, and shots using

Scl-1 CPP's driven with a 2.8 ns, 3 ns, and 5 ns drive are shown in Fig. 11. Zn, Ge, and Br data are shown in green, orange, and magenta curves, respectively. Laser arrival times are monitored at NIF; for backlighter experiments beam arrival times varied between 3 to 80 ps later or 7 to 30 ps earlier than the nominal laser t=0. Black curves represent the main laser drive with nominal timing. Dedicated timing shots at NIF demonstrate DISC is timed to within ± 50 ps of the requested time relative to the facility's master trigger. To compare between different experimental configurations, DISC's counts per pixel were normalized to a 5-ns sweep speed, 9X magnification, 17 μ m imaging-slit setup. Here data are smoothed using a median method to avoid outlying points from dominating the data trends.

Figure 11 (a) shows temporal emission for highest irradiance Zn and Ge shots. These used 400 μ m CPP's driven with a nominally 3.0 ns (Zn) and 2.8 ns (Ge) main drive, shown as the dotted and solid smooth curves, respectively. The 5 μ m Zn foil begins to emit ~ 250 ps after the main laser drive begins, decaying after reaching maximum emission, indicative of foil burn through. Ge foils display comparable delay times between the laser main drive and emission rise time, on the order of 150-300 ps. Here rise time is defined as the temporal location half way between no emission and peak emission on the rising edge. Around 800 ps after emission rise time, the Ge foil emission reaches a steady state that lasts until the end of the main drive, quickly decaying once the laser is off.

Ge and Br foils using Scl-1 CPP's with either a 2.8 ns or 3.0 ns main drive, Fig. 11 (b) and (c) respectively, reach an emission plateau ~ 400 -500 ps after the emission rise time. A delay time between emission signal and main laser drive is also measured, ~ 250 ps and ~ 400 ps for the 2.8 ns and 3.0 ns main drive cases. Figure 11 (d) show results for shots using a 5 ns drive with Scl-1 CPP's, corresponding to several laser irradiances. For this set of shots the rising phase of the foil emission is outside the sweep window. The solid and dotted data curves correspond to 0.57 and 1.1 $\times 10^{15}$ W/cm² laser irradiance. Zn data shows a thicker 15 μ m foil produces a more temporally stable emission in comparison to the 5 μ m foil. At this irradiance the 5 μ m foil also burns through, as indicated by its measured emission. DISC records ~ 4000 counts per pixel over ~ 600 ps for the 5 μ m foil, and ~ 3000 counts per pixel for the 15 μ m foil, which is steady over ~ 4 ns. Both the Ge and Br shots show steady emission.

4. Conclusions

Laser-to-x-ray conversion efficiency was measured on the National Ignition Facility for Zn, Ge, Br, and Zr planar foils using a time-integrated x-ray spectrometer, the Dante diagnostic, and an imaging, filtered x-ray streak camera. The foils were driven with peak laser irradiances varying from 0.57 to 9.5 $\times 10^{15}$ W/cm². Absolute x-ray line emission into He $_{\alpha}$ plus satellites was measured using the SuperSnout II spectrometer. Dante measurements provided a second absolute measurement, though with coarse spectral resolution. The temporal behavior of the broadband x-ray emission from the backlighter and a relative CE were measured with the DISC x-ray streak camera.

Targets were driven with a constant-power main drive pulse that had a pre-pulse to create underdense plasma conditions allowing better coupling of the main laser drive energy into thermal energy of the target. Peak CE's for Ge foils were measured at 1.5% into He $_{\alpha}$ plus satellite emission and 2% into a broadband x-ray emission. This is significantly higher than that measured in previous studies using higher laser irradiances and no laser pre-pulse. CE enhancement was also observed for Zn foils in comparison to previous studies, although a full mapping of CE as a function of laser irradiance for absolute measurements was not possible due to limited shot allocation. A 1% CE into Zn He $_{\alpha}$ and 1.5% broadband CE were recorded for Zn, though these do not correspond to optimized conditions. CE from a KBr film was the lowest measured at 0.3% into He $_{\alpha}$ line emission, and

0.8% into broadband. These results are encouraging, and warrant further work to find conditions where Br He α emission is optimized. Future work will use RbBr films, where the He α emission from the Rb and Br x-ray emission can be measured within a single narrow spectral window. Finally, x-ray output was recorded for Zr foils, with the highest values being 0.43% for the broadband CE and 0.4% CE into He α plus satellite emission. These results show that high-Z materials are viable backlighter sources and can be further optimized.

DISC measurements show the 5 μ m Zn foils have a rapidly decaying emission as a function of time at measured irradiances greater than 0.5×10^{15} W/cm 2 , indicating burn through of the foil. The thicker Zn, Ge, and Br targets are relatively steady over the main laser drive pulse, with emission dropping soon after the laser has turned off. A time delay between the start of the main laser drive and observed emission on the DISC detector is observed for all the foils, and is of the order of 300 ps. Relative CE derived from DISC measurements and absolute CE into He α line emission are consistent with $(h\nu)^{-3}$ to $(h\nu)^{-5}$ scaling.

Laser pre-pulse intensity levels were not systematically investigated in this study. They were only modified between Scl-1 and 400 μ m CPP's to prevent premature foil burn through. Pre-pulse conditions were based on previous experiments on thin Ge foils. Stronger pre-pulse power is likely needed for higher Z materials like Br and Zr in order to achieve similar pre-formed plasma conditions as those in Ge and Zn. Efforts are currently underway to simulate the hydrodynamics of these laser-produced plasma and to predict the x-ray spectra using detailed atomic physics codes. Future experiments will investigate optimized planar foil backlighter designs and test higher Z material.

Acknowledgements

The authors thank the operations crew at NIF for their effort and support for these experiments. This work was done under the auspices of the U. S. Department of Energy by Lawrence Livermore National Laboratory under Contract DE-AC52-07NA27344.

References

- [1] J. Hawreliak, H. E. Lorenzana, B. A. Remington, S. Lukezic, and J. S. Wark, "Nanosecond x-Ray diffraction from polycrystalline and amorphous materials in a pinhole camera geometry suitable for laser shock compression experiments," *Review of Scientific Instruments* **78**(8), 083908–083908–6 (2007) [doi:doi:10.1063/1.2772210].
- [2] C. C. Kuran, R. P. Drake, M. J. Grosskopf, H. F. Robey, B. A. Remington, J. F. Hansen, B. E. Blue, and J. Knauer, "Image processing of radiographs in 3D Rayleigh-Taylor decelerating interface experiments," *Astrophys Space Sci* **322**(1-4), 49–55 (2009) [doi:10.1007/s10509-008-9967-4].
- [3] A. B. Reighard and R. P. Drake, "The Formation of a Cooling Layer in a Partially Optically Thick Shock," *Astrophys Space Sci* **307**(1-3), 121–125 (2007) [doi:10.1007/s10509-006-9237-2].
- [4] C. A. Back, T. S. Perry, D. R. Bach, B. G. Wilson, C. A. Iglesias, O. L. Landen, S. J. Davidson, and B. J. B. Crowley, "Opacity measurements: Extending the range and filling in the gaps," *Journal of Quantitative Spectroscopy and Radiative Transfer* **58**(4–6), 415–425 (1997) [doi:10.1016/S0022-4073(97)00049-6].
- [5] F. Gilleron, H. Merdji, M. Fajardo, O. Henrot, J. C. Gauthier, C. Chénais-Popovics, W. Fölsner, and K. Eidmann, "LTE absorption spectroscopy of an X-ray heated boron plasma," *Journal of Quantitative Spectroscopy and Radiative Transfer* **69**(2), 217–229 (2001) [doi:10.1016/S0022-4073(00)00078-9].

- [6] S. J. Davidson, J. M. Foster, C. C. Smith, K. A. Warburton, and S. J. Rose, "Investigation of the opacity of hot, dense aluminum in the region of its K edge," *Applied Physics Letters* **52**(10), 847–849 (1988) [doi:doi:10.1063/1.99304].
- [7] B. R. Maddox, H.-S. Park, J. Hawreliak, A. Elsholz, R. Van Maren, B. A. Remington, A. Comley, and J. S. Wark, "Bragg diffraction using a 100 ps 17.5 keV x-ray backlighter and the Bragg diffraction imager," *Review of Scientific Instruments* **81**(10), 10E522–10E522–3 (2010) [doi:doi:10.1063/1.3491295].
- [8] D. G. Hicks, N. B. Meezan, E. L. Dewald, A. J. Mackinnon, R. E. Olson, D. A. Callahan, T. Döppner, L. R. Benedetti, D. K. Bradley, et al., "Implosion dynamics measurements at the National Ignition Facility," *Physics of Plasmas* **19**(12), 122702–122702–26 (2012) [doi:doi:10.1063/1.4769268].
- [9] G. H. Miller, E. I. Moses, and C. R. Wuest, "The National Ignition Facility: enabling fusion ignition for the 21st century," *Nuclear Fusion* **44**(S228) (2004).
- [10] G. H. Miller, E. I. Moses, and C. R. Wuest, *Opt. Eng.* **443**(284) (2004).
- [11] J. Dunn, B. K. Young, A. L. Osterheld, M. E. Foord, R. S. Walling, R. E. Stewart, and A. Y. Faenov, "Spectroscopic investigations of hard x-ray emission from 120-ps laser-produced plasmas at intensities near 1017 W cm⁻²," *Proc. SPIE* **2523**, 254–263 (1995) [doi:10.1117/12.220986].
- [12] S. G. Glendinning, P. A. Amendt, K. S. Budil, B. A. Hammel, D. H. Kalantar, M. H. Key, O. L. Landen, B. A. Remington, and D. E. Desenne, "Laser plasma diagnostics of dense plasmas," *Proc. SPIE* **2523**, 29–39 (1995) [doi:10.1117/12.220989].
- [13] J. Workman and G. A. Kyrala, "X-ray yield scaling studies performed on the OMEGA laser," *Review of Scientific Instruments* **72**(1), 678–681 (2001) [doi:doi:10.1063/1.1318251].
- [14] J. Workman and G. A. Kyrala, "Scaling of x-ray K-shell sources from laser-solid interactions," presented at Society of Photo-Optical Instrumentation Engineers (SPIE) Conference Series, 1 November 2001, 168–179.
- [15] A. Akkerman, A. Gibrekhterman, A. Breskin, and R. Chechik, "Monte Carlo simulations of secondary electron emission from CsI, induced by 10 keV x rays and electrons," *Journal of Applied Physics* **72**(11), 5429–5436 (1992) [doi:10.1063/1.351984].
- [16] D. G. Hicks, B. K. Spears, D. G. Braun, R. E. Olson, C. M. Sorce, P. M. Celliers, G. W. Collins, and O. L. Landen, "Convergent ablator performance measurements," *Physics of Plasmas* **17**(10), 102703–102703–11 (2010) [doi:doi:10.1063/1.3486536].
- [17] D. G. Hicks, B. K. Spears, D. G. Braun, R. E. Olson, C. M. Sorce, P. M. Celliers, G. W. Collins, and O. L. Landen, "Streaked radiography measurements of convergent ablator performance (invited)," *Review of Scientific Instruments* **81**(10), 10E304–10E304–5 (2010) [doi:doi:10.1063/1.3475727].
- [18] Y. Lin, T. J. Kessler, and G. N. Lawrence, "Distributed phase plates for super-Gaussian focal-plane irradiance profiles," *Opt. Lett.* **20**(7), 764–766 (1995) [doi:10.1364/OL.20.000764].
- [19] C. A. Back, J. Davis, J. Grun, L. J. Suter, O. L. Landen, W. W. Hsing, and M. C. Miller, "Multi-keV x-ray conversion efficiency in laser-produced plasmas," *Physics of Plasmas* **10**(5), 2047–2055 (2003) [doi:doi:10.1063/1.1566750].
- [20] F. Girard, J. P. Jadaud, M. Naudy, B. Villette, D. Babonneau, M. Primout, M. C. Miller, R. L. Kauffman, L. J. Suter, et al., "Multi-keV x-ray conversion efficiencies of laser-preexploded titanium foils," *Physics of Plasmas* **12**(9), 092705 (2005) [doi:10.1063/1.2032167].

- [21] C. A. Back, J. Grun, C. Decker, L. J. Suter, J. Davis, O. L. Landen, R. Wallace, W. W. Hsing, J. M. Laming, et al., "Efficient Multi-keV Underdense Laser-Produced Plasma Radiators," *Phys. Rev. Lett.* **87**(27), 275003 (2001) [doi:10.1103/PhysRevLett.87.275003].
- [22] D. Babonneau, M. Primout, F. Girard, J.-P. Jadaud, M. Naudy, B. Villette, S. Depierreux, C. Blancard, G. Faussurier, et al., "Efficient multi-keV X-ray sources from laser-exploded metallic thin foils," *Physics of Plasmas* **15**(9), 092702–092702–15 (2008) [doi:doi:10.1063/1.2973480].
- [23] F. Girard, J.-P. Jadaud, M. Naudy, B. Villette, D. Babonneau, M. Primout, S. Depierreux, M. C. Miller, R. L. Kauffman, et al., "Multi-keV x-ray conversion from prepulsed foil experiments," *SPIE* **5196**, 220–233 (2004) [doi:10.1117/12.510010].
- [24] S. P. Regan, M. A. Barrios, K. B. Fournier, J. D. Kilkenny, J. Emig, C. Bailey, P. Bell, D. K. Bradley, M. Bedzyk, et al., "Supersnout II diagnostic for the National Ignition Facility," *to be submitted to RSI*.
- [25] B. L. Henke, H. T. Yamada, and T. J. Tanaka, "Pulsed plasma source spectrometry in the 80–8000-eV x-ray region," *Review of Scientific Instruments* **54**(10), 1311–1330 (1983) [doi:doi:10.1063/1.1137264].
- [26] M. J. Haugh, S. P. Regan, K. D. Jacoby, P. W. Ross, J. Magoon, M. A. Barrios, J. A. Emig, M. J. Shoup, and K. B. Fournier, "Integrated x-ray reflectivity measurements of elliptically curved pentaerythritol crystals," *Review of Scientific Instruments* **83**(10), 10E122–10E122–3 (2012) [doi:doi:10.1063/1.4738748].
- [27] B. R. Maddox, H. S. Park, B. A. Remington, N. Izumi, S. Chen, C. Chen, G. Kimminau, Z. Ali, M. J. Haugh, et al., "High-energy x-ray backlighter spectrum measurements using calibrated image plates," *Review of Scientific Instruments* **82**(2), 023111–023111–10 (2011) [doi:doi:10.1063/1.3531979].
- [28] M. J. May, K. Widmann, C. Sorce, H.-S. Park, and M. Schneider, "Uncertainty analysis technique for OMEGA Dante measurements," *Review of Scientific Instruments* **81**(10), 10E505–10E505–3 (2010) [doi:doi:10.1063/1.3475385].
- [29] C. Sorce, J. Schein, F. Weber, K. Widmann, K. Campbell, E. Dewald, R. Turner, O. Landen, K. Jacoby, et al., "Soft x-ray power diagnostic improvements at the Omega Laser Facility," *Review of Scientific Instruments* **77**(10), 10E518–10E518–4 (2006) [doi:doi:10.1063/1.2336462].
- [30] K. M. Campbell, F. A. Weber, E. L. Dewald, S. H. Glenzer, O. L. Landen, R. E. Turner, and P. A. Waide, "Omega Dante soft x-ray power diagnostic component calibration at the National Synchrotron Light Source," *Review of Scientific Instruments* **75**(10), 3768–3771 (2004) [doi:doi:10.1063/1.1789603].
- [31] J. R. Kimbrough, P. M. Bell, D. K. Bradley, J. P. Holder, D. K. Kalantar, A. G. MacPhee, and S. Telford, "Standard design for National Ignition Facility x-ray streak and framing cameras," *Review of Scientific Instruments* **81**(10), 10E530–10E530–3 (2010) [doi:doi:10.1063/1.3496990].
- [32] Y. P. Opachich, N. Palmer, D. Homoelle, B. Hatch, P. Bell, D. Bradley, D. Kalantar, D. Browning, J. Zuegel, et al., "X-ray streak camera cathode development and timing accuracy of the 4 ω ultraviolet fiducial system at the National Ignition Facility," *Review of Scientific Instruments* **83**(10), 10E123–10E123–3 (2012) [doi:doi:10.1063/1.4732855].
- [33] Y. P. Opachich, D. H. Kalantar, A. G. MacPhee, J. P. Holder, J. R. Kimbrough, P. M. Bell, D. K. Bradley, B. Hatch, G. Brienza-Larsen, et al., "High performance imaging streak camera for the National Ignition Facility," *Review of Scientific Instruments* **83**(12), 125105–125105–6 (2012) [doi:doi:10.1063/1.4769753].
- [34] H. R. Griem, *Principles of Plasma Spectroscopy*, Cambridge University Press (1997).

- [35] M. J. May, J. R. Patterson, C. Sorce, K. Widmann, K. B. Fournier, and F. Perez, "Source geometric considerations for OMEGA Dante measurements," *Review of Scientific Instruments* **83**(10), 10E117–10E117–3 (2012) [doi:doi:10.1063/1.4734041].
- [36] F. Girard, M. Primout, B. Villette, P. Stemmler, L. Jacquet, D. Babonneau, and K. B. Fournier, "Titanium and germanium lined hohlraums and halfraums as multi-keV x-ray radiators," *Physics of Plasmas* **16**(5), 052704–052704–11 (2009) [doi:doi:10.1063/1.3130263].
- [37] F. Girard, M. Primout, B. Villette, P. Stemmler, L. Jacquet, D. Babonneau, and K. B. Fournier, "Erratum: 'Titanium and germanium lined hohlraums and halfraums as multi-keV x-ray radiators' [Phys. Plasmas 16, 052704 (2009)]," *Physics of Plasmas* **18**(7), 079901–079901–1 (2011) [doi:doi:10.1063/1.3600532].
- [38] K. B. Fournier, J. H. Satcher, M. J. May, J. F. Poco, C. M. Sorce, J. D. Colvin, S. B. Hansen, S. A. MacLaren, S. J. Moon, et al., "Absolute x-ray yields from laser-irradiated germanium-doped low-density aerogels," *Physics of Plasmas* **16**(5), 052703–052703–13 (2009) [doi:doi:10.1063/1.3140041].
- [39] J. Workman, J. R. Fincke, P. Keiter, G. A. Kyrala, T. Pierce, S. Sublett, J. P. Knauer, H. Robey, B. Blue, et al., "Development of intense point x-ray sources for backlighting high energy density experiments (invited)," *Review of Scientific Instruments* **75**(10), 3915–3920 (2004) [doi:doi:10.1063/1.1789248].
- [40] T. Boutboul, A. Akkerman, A. Gibrekhterman, A. Breskin, and R. Chechik, "An improved model for ultraviolet- and x-ray-induced electron emission from CsI," *Journal of Applied Physics* **86**(10), 5841–5849 (1999) [doi:doi:10.1063/1.371601].
- [41] I. Frumkin, A. Breskin, R. Chechik, V. Elkind, and A. Notea, "Properties of CsI-based gaseous secondary emission X-ray imaging detectors," *Nuclear Instruments and Methods in Physics Research Section A: Accelerators, Spectrometers, Detectors and Associated Equipment* **329**(1–2), 337–347 (1993) [doi:10.1016/0168-9002(93)90952-E].
- [42] A. Gibrekhterman, A. Akkerman, A. Breskin, and R. Chechik, "Characteristics of secondary electron emission from CsI induced by x rays with energies up to 100 keV," *Journal of Applied Physics* **74**(12), 7506–7509 (1993) [doi:doi:10.1063/1.354975].

Figure Captions

Figure 1 (Color online) The laser power incident on the planar foil targets consists of a pre-pulse fired 3 ns in advance of the main square pulse, with temporal duration between 2 to 5 ns. The laser pre-pulse creates an under dense plasma resulting in higher measured CE.

Figure 2 (Color online) Laser-irradiated foil conditions were characterized using a suite of x-ray diagnostics. The time-integrated x-ray spectrum in the 6-16 keV range was recorded with the SSIIS from the (θ, ϕ) direction of $(0^\circ, 0^\circ)$. The filtered photodiode array of the Dante diagnostic recorded the broadband x-ray emission in the 0.5 to 20 keV range from the $(143^\circ, 274^\circ)$ direction. A time-resolved and 1-D spatially-resolved image of the x-ray emission was recorded with an x-ray streak camera (DISC) from the $(90^\circ, 78^\circ)$ direction, opposite the drive beams.

Figure 3 (Color online) Compilation of time-integrated x-ray emission above 6 keV measured using a static x-ray imager. (a) Nearly side-on view of foil targets as viewed with the static x-ray imager located at (θ, ϕ) of $(161^\circ, 236^\circ)$, observing the plasma plume expansion. (b) Recorded x-ray emission from the plasma plume for various laser configurations. From left to right: Spatially separated Scl-1 and 400 μ m CPP's using nominal 3 ns main drive with four overlapping beams per configuration, Scl-1 CPP's with 3ns and 5 ns main drives at different target locations with four beams per configuration, and Scl-1 CPP's with nominal 2 ns drive using eight overlapping beams. The plasma size parallel to the surface is closely related to the laser spot size. The plasma plume expansion, perpendicular to the target surface, varies between Scl-1 and 400 μ m CPP's and is of the order of hundreds of microns at its farthest point.

Figure 4 (Color online) Time-integrated and spatially-integrated spectra measured with the 3in the 8 to 16 keV photon energy range for (a) Zn, (b) Ge, and (c) Br targets, show He-like emission dominates K-shell spectra for these materials. Results from individual spectrometer channels are shown as the dotted (ch.1), dashed (ch.2), dot-dashed (ch.3), and solid (ch4.) curves.

Figure 5 (Color online) Time- and spatially-integrated Zr He_α line emission profile, measured in second order Bragg reflection, after subtraction of local continuum using SSIIS channels 1, 2, and 3, shown as dotted, dashed, and dot-dashed curves.

Figure 6 (Color online) Laser-to-x-ray conversion efficiencies for the He_α and satellite emission as measured with SSIIS for Zn, Ge, Br, and Zr planar targets are shown as the filled diamond, squares, triangle, and circles, respectively. Previous work for Zn and Ge planar foils having similar target thickness, but no pre-pulse are shown as the unfilled symbols. A comparison of the results from the previous work with this study indicates a higher CE is achieved at lower laser irradiance for the Zn and Ge foils using a pre-pulse.

Figure 7 (Color online) Line and continuum CE as measured with Dante and the SSIIS. Dante (SSIIS) data for Zn, Ge, Br, and Zr are shown as the filled (unfilled) diamonds, - filled (unfilled) squares, - filled (unfilled) triangle, and - filled (unfilled) circles.

Figure 8 (Color online) Compilation of previous work measuring laser-to-x-ray conversion efficiencies, compared to SSIIS (CE into He_α) results from this study. NIF pre-pulse foils outperform previous hohlraum/halfraum (rectangles), aerogel (diamonds), and single-

drive foil (downward triangles) targets. The experiment laser irradiance is indicated by color. Experiments with unknown laser irradiance are unfilled.

Figure 9 (Color online) Relative laser-to-x-ray conversion efficiency from DISC measurements show increasing x-ray output for increasing laser irradiance.

Figure 10 (Color online) X-ray to laser conversion efficiency scaling with He_α photon energy, as measured with DISC for fixed laser irradiance is consistent with $(h\nu)^{-3}$ to $(h\nu)^{-5}$. Filled diamonds, squares, and triangles, represent Zn, Ge, and KBr measurements.

Figure 11 (Color online) DISC traces showing temporal uniformity of backlighter foils for five different main laser drives, each shown as the solid smooth curve in TW per beam on the right hand axis: (a) 2.8 ns main drive with 400 μm CPP's (solid smooth curve), for two Ge shots (solid light curve) and a 400 μm CPP's driven with a nominally 3.0 (upper dashed smooth curve) for one Zn shot (dashed curve); (b) 2.8 ns main drive for two Ge shots (solid light curve); (c) 3.0 ns main drive for one Ge shot (upper light curve) and one Br shot (lower darker curve); and, (d) 5.0 ns main drive all with Scl-1 CPP's for two Zn shots (denoted by 5 μm and 15 μm), three Ge shots (denoted by the upper dashed curve and the two lower solid curve), and one Br shot (Lower dashed curve). DISC counts per pixel, left axis, are normalized to a 5-ns sweep speed, 9X magnification, with 17 μm imaging-slit setup.

Tables

Table 1. Foil thickness and characteristic energy of He_α line emission are listed for materials tested in this study.

	Zn	Ge*	Br†	Zr
He_α (keV)	8.9	10.3	12.3	16.3
Foil thickness	5 μm or 15 μm	10-12 μm	10-12 μm	7 μm

* Ge foil on 200 μm of graphite.

† KBr film on 25 μm Al substrate.

Table 2. Electron-temperature estimates obtained from the time-integrated L-shell recombination continuum measured using SSIIS, modeled as $I_0 e^{-h\nu/T}$. Errors include fitting parameters and variation among overlapping spectrometer channels.

Shot No.	Foil	T_e (keV)	δT_e (keV)
N120416-001	Ge	2.09	0.07
N120616-001	Zn	0.87	0.01
N120709-001	Ge	1.36	0.04
N120812-001	Ge	1.55	0.01
N120812-003	Br	1.49	0.02
N120916-002	Ge	1.53	0.03
N130324-002	Zn	0.85	0.01
N130324-003	Zn	0.84	0.06

Table 3. Laser-to-x-ray conversion efficiency (CE), defined as emitted x-rays over total energy imparted onto the target, calculated for various backlighter foils using SSIS and Dante diagnostics. SSIS spectral resolution allows calculation of CE exclusively into He_α , as well as a relatively broadband measurement between 8 to 16 keV. Measurement errors, where available, shown in parentheses.

Shot No.	Foil	$I_{\text{NIF}} \times 10^{15}$ (W/cm ²)	$\text{CE}_{\text{SSIS}}(\%)$ (He_α)	$\text{CE}_{\text{Dante}}(\%)$ (He_α)	$\text{CE}_{\text{SSIS}}(\%)$ (8.5-16.5 keV)	$\text{CE}_{\text{Dante}}(\%)$ (8.5-16.5 keV)
N120616-001	Zn	0.57	0.62(0.19)	0.92(0.05)	0.88(0.23)	1.10(0.05)
N130324-002	Zn	1.96	1.08(0.26)	1.68(0.08)	1.53(0.40)	2.20(0.11)
N130324-003	Zn	3.50	0.69(0.16)	0.91(0.05)	1.0(0.26)	1.18(0.06)
N120227-004	Zn	5.35	n/a	1.00(0.05)	n/a	1.30(0.06)
N120709-001	Ge	0.57	0.52(0.11)	0.64(0.04)	0.89(0.23)	0.68(0.03)
N120812-001	Ge	1.45	1.54(0.31)	1.26(0.07)	2.61(0.68)	1.37(0.07)
N120417-001	Ge	1.65	n/a	1.17(0.06)	n/a	1.45(0.07)
N120713-002	Ge	1.82	n/a	1.36(0.07)	n/a	1.42(0.07)
N120916-002	Ge	1.94	1.28(0.37)	1.20(0.07)	2.23(0.58)	1.38(0.07)
N120416-001	Ge	2.96	0.64(0.18)	1.2(0.07)	1.23(0.32)	1.39(0.07)
N120417-001	Ge	4.27	n/a	0.53(0.03)	n/a	0.59(0.03)
N120812-003	Br	1.45	0.29(0.09)	n/a	0.80(0.21)	0.52(0.03)
N121203-001	Zr	1.90	0.40(0.22)	n/a	n/a	0.43(0.02)
N121115-001	Zr	9.53	0.32(0.13)	n/a	n/a	0.36(0.02)

Figures

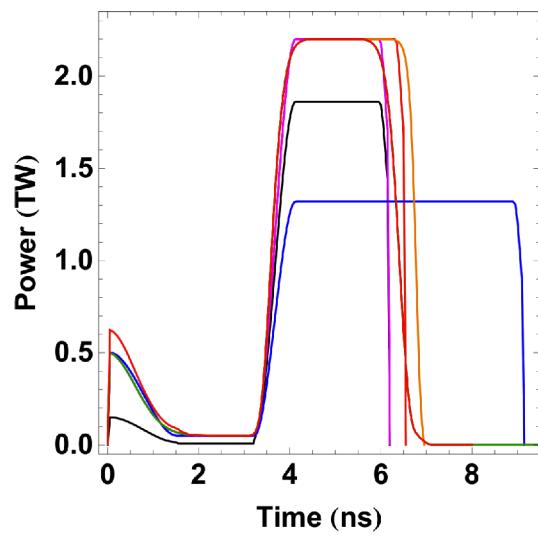


Fig. 1

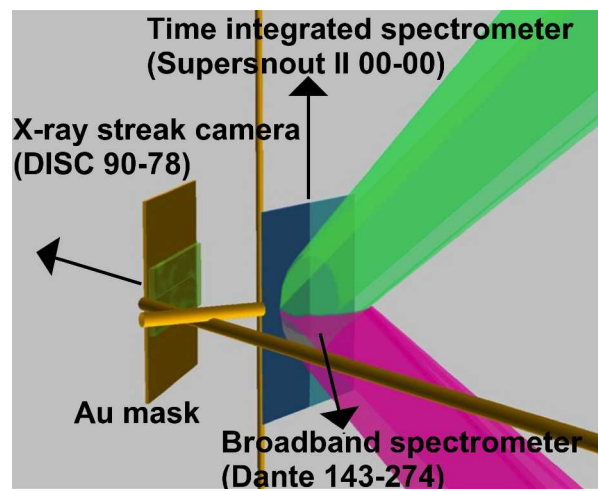


Fig. 2

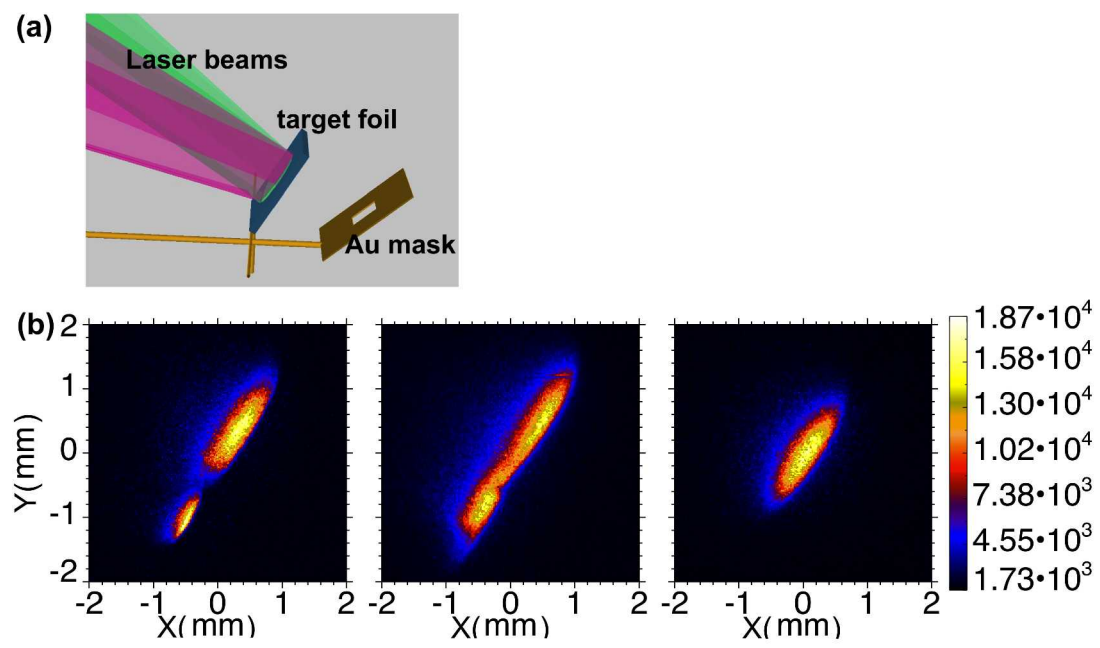


Fig. 3

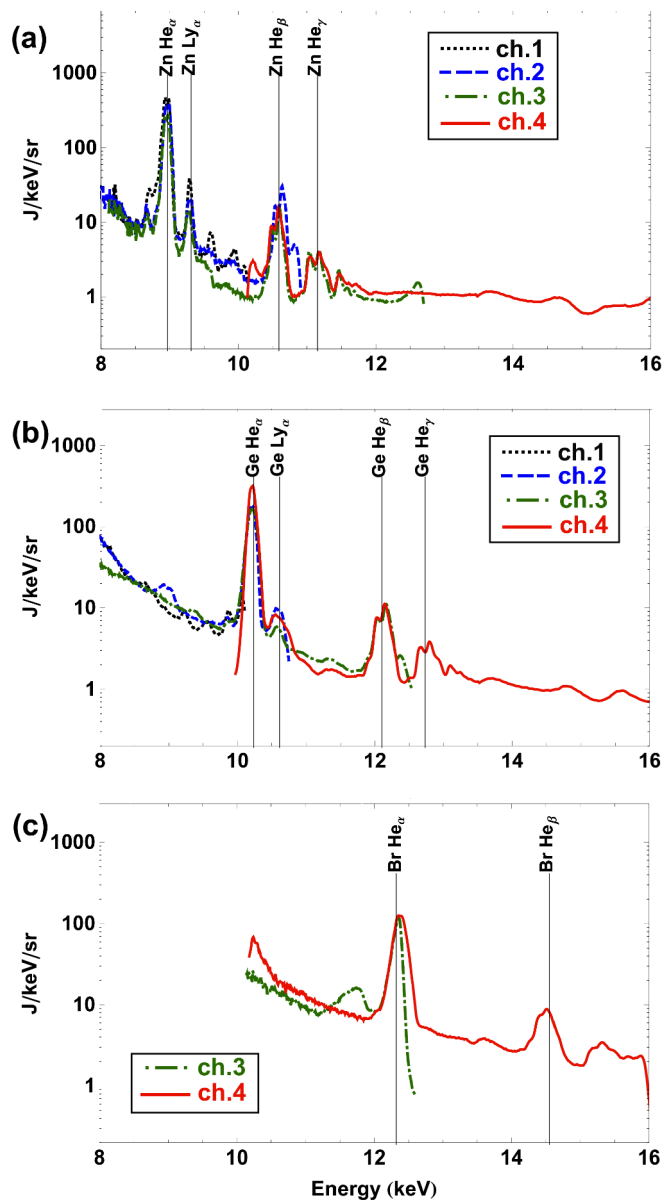


Fig. 4

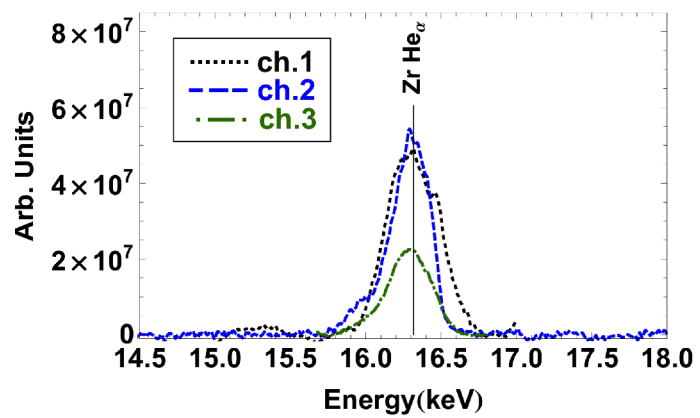


Fig. 5

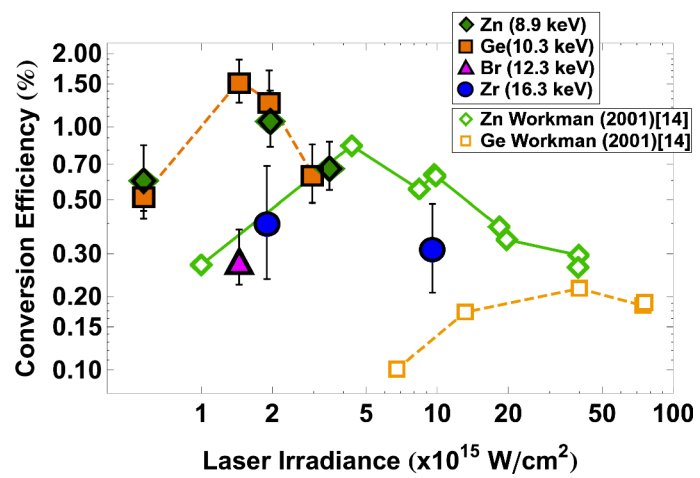


Fig. 6

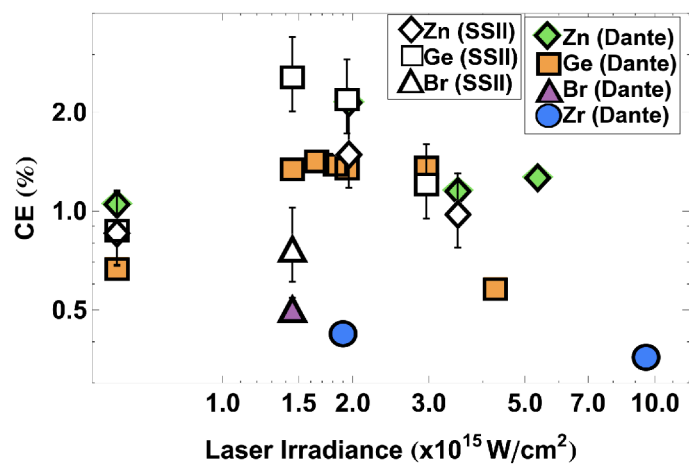


Fig. 7

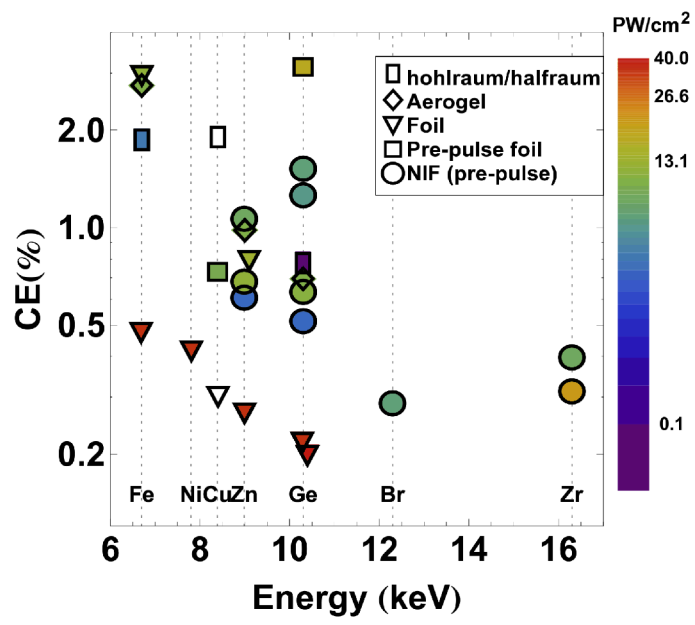


Fig. 8

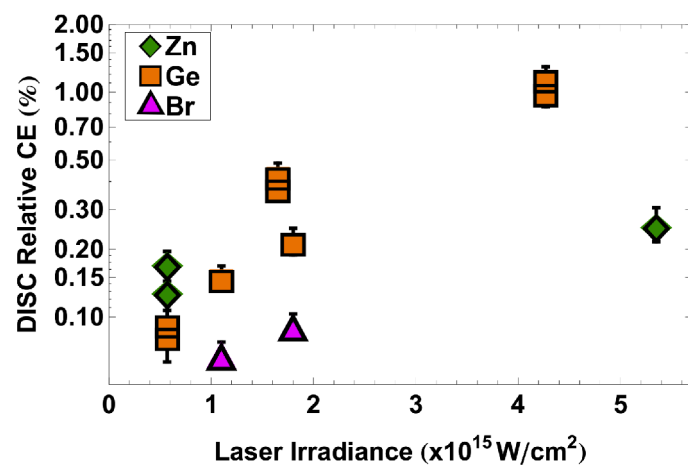


Fig. 9

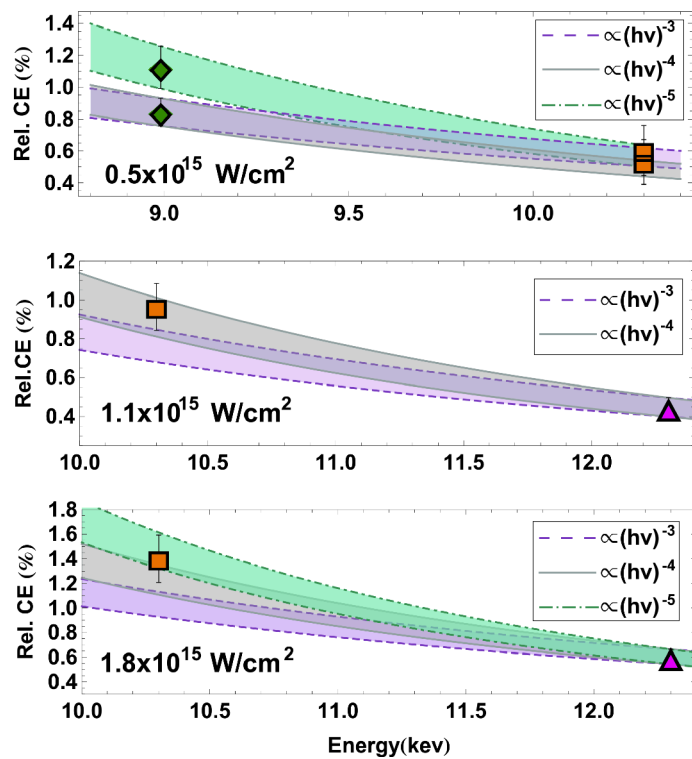


Fig. 10

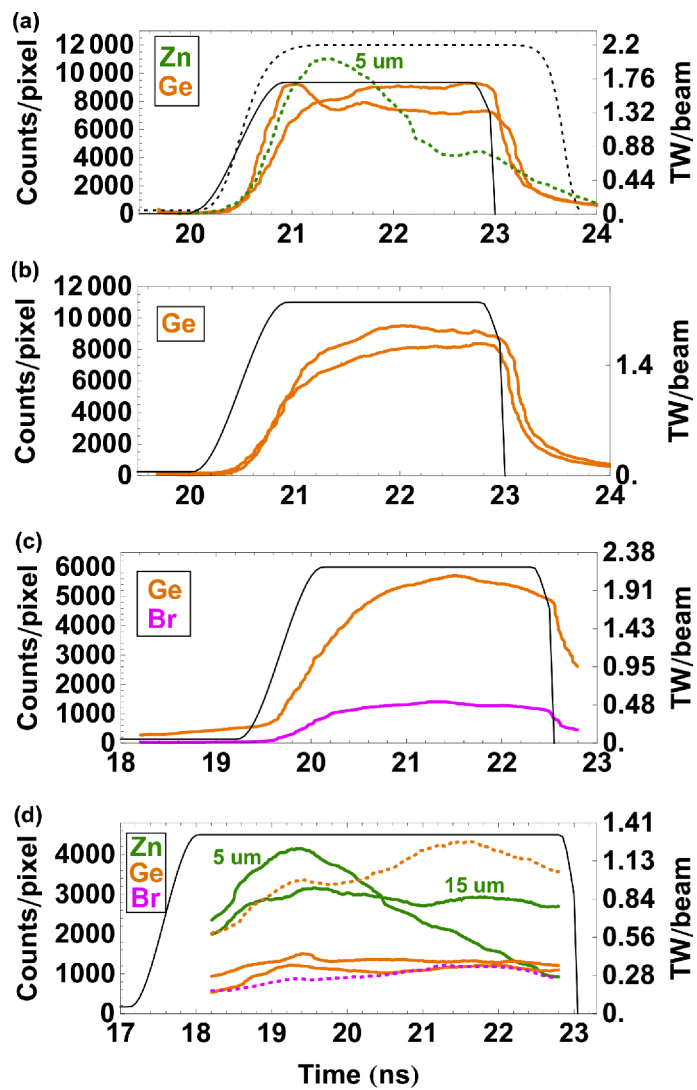


Fig. 11